Sustainable Energy, Grids and Networks 42 (2025) 101699

Contents lists available at ScienceDirect

Sustainable Energy, Grids and Networks

journal homepage: www.elsevier.com/locate/segan

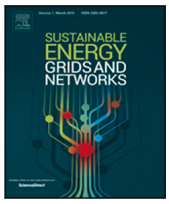

Sizing of Fast Frequency Response Reserves for improving frequency security in low-inertia power systems

Savvas Panagi [a,b,*], Petros Aristidou [b]

[a] Distribution System Operator, Electricity Authority of Cyprus, Amfipoleos 11, Nicosia, 1399, Cyprus
[b] Electrical & Computer Engineering, & Informatics, Cyprus University of Technology, Archiepiskopou Kyprianou 30, Limassol, 3036, Cyprus

ARTICLE INFO

Keywords:
Fast Frequency Response (FFR)
BESS sizing
Frequency security
Low-inertia grids

ABSTRACT

The increasing penetration of Renewable Energy Sources (RES) in electricity grids has led to the gradual decommissioning of conventional generators and, thus, to a decrease in the available inertia and other frequency support reserves. Consequently, the frequency security of power systems, in particular islanded low-inertia ones, is compromised, leading to faster and more extreme frequency deviations following disturbances. There is an urgent need to incorporate faster frequency reserves that can stabilize the system and enhance its resilience and reliability. This paper first investigates the impact of various frequency support mechanisms on the system frequency security in low-inertia grids. Then, we propose a novel, data-driven, gradient-descent-based method, that combines Dynamic Security Assessment (DSA) with linear predictions to optimize Fast Frequency Response (FFR) sizing for low-inertia grids. The performance of the proposed approach is evaluated using the dynamic model of Cyprus across 500 selected historical operating scenarios. The results demonstrate fast convergence, achieving the target frequency Nadir with minimal computational effort.

1. Introduction

In electric power systems, the power generated must always be balanced against the power consumed at any given moment. Any deviation from this equilibrium results in a power imbalance that directly affects the rotational speed of synchronous generators, causing deviations in the electrical frequency of the system. This relationship is described by the swing equation, which models the dynamics of rotor motion in response to active power variations [1]. Large power imbalances frequently arise in power systems due to unexpected interruptions in production or consumption, commonly referred to as *disturbances*, resulting in significant frequency deviations. Their nature depends on the pre-disturbance operating conditions, the size, type, and location of the disturbance, and the available frequency support reserves.

Fig. 1 illustrates the post-disturbance frequency response following a loss of generation under different operating conditions. The main characteristics of the post-disturbance frequency related to security are the initial Rate of Change of Frequency (RoCoF), the frequency Nadir, and the steady-state post-fault frequency. Transmission System Operators (TSOs) are usually responsible for ensuring sufficient frequency support reserves [2,3] to maintain a secure post-disturbance frequency response.

Traditional power grids heavily rely on large power plants that use synchronous generators (SG) to provide Kinetic Energy (KE) and Frequency Containment Reserves (FCR) to ensure post-disturbance frequency security. However, to achieve the sustainability goals set by world governments [4] and reduce dependence on fossil fuels, the penetration of RES is constantly increasing, leading to the decommissioning of conventional power plants (SG-based). Consequently, this reduces the available KE and FCR and causes significant frequency regulation challenges, especially in low-inertia power systems [1,3]. More specifically, the post-disturbance frequency behavior of the system deteriorates, leading to a worsened RoCoF, Nadir and post-fault steady-state frequency. This is shown graphically in Fig. 1, which illustrates the impact of the increasing RES penetration on the post-fault system frequency response in Cyprus. In all the scenarios presented in this figure, the load consumption remained the same, while the only changes were in the available FCR and the KE due to the decommissioning of conventional generators.

To address this problem, various technologies and solutions have been investigated over the years [5,6]. The use of Battery Energy Storage Systems (BESS) has been proposed to provide the necessary frequency support due to their speed of response, adaptability, and

* Corresponding author at: Electrical & Computer Engineering, & Informatics, Cyprus University of Technology, Archiepiskopou Kyprianou 30, Limassol, 3036, Cyprus.
E-mail address: savvas.panagi@cut.ac.cy (S. Panagi).

https://doi.org/10.1016/j.segan.2025.101699
Received 8 October 2024; Received in revised form 22 February 2025; Accepted 24 March 2025
Available online 4 April 2025

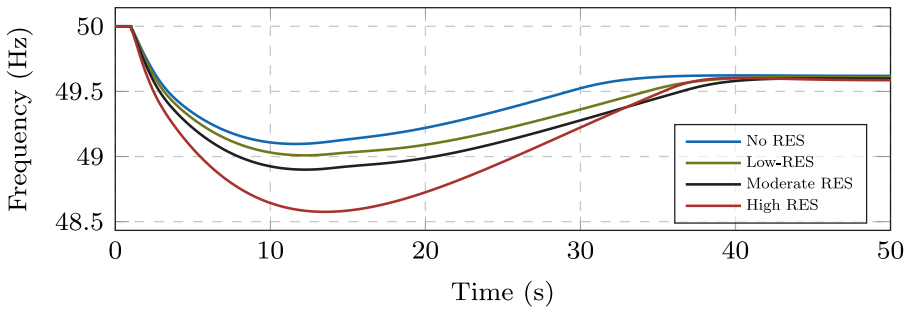

Fig. 1. Post-disturbance frequency response for different RES levels.

robustness [5,6]. Consequently, many TSOs are considering Fast Frequency Response (FFR) reserves through BESS as a new support service to mitigate post-disturbance frequency-related challenges. In some countries, system operators have already incorporated FFR into their grid codes as a reserve service to enhance frequency regulation. For instance, FFR was implemented in the Nordics in May 2020 [7], in Cyprus at the end of 2024 [8], in Australia at the end of 2023 [9], and in Ireland (EirGrid). Two primary categories of FFR control methods are employed: (1) droop-based control, where the response of the BESS is proportional to the frequency deviation or RoCoF; and (2) step-change response, where FFR is activated upon reaching a predefined frequency or RoCoF threshold.

1.1. Objectives

One of the key challenges when introducing FFR services, as addressed in this work, is determining the power (MW) and energy (MWh) capacity of the BESS required to provide the necessary support. While sizing the BESS to provide KE, if applicable, and FCR is relatively straightforward due to the linear nature of frequency dynamics related to the RoCoF and post-fault steady-state frequency (see Section 2 of [10]), the frequency dynamics associated with the frequency Nadir are highly non-linear. This non-linearity makes the BESS sizing process for improving the Nadir through FFR significantly more complex.

This work proposes a novel, data-driven methodology to optimize FFR sizing for low-inertia grids. The proposed method integrates DSA with a linear FFR power estimator utilizing a gradient descent-based approach to determine the required FFR capacity that ensures the frequency Nadir remains within acceptable limits. Additionally, this study aims to demonstrate the fast convergence and effective performance of the proposed approach, minimizing computational overhead while achieving the target frequency response. Another key objective is to enable TSOs to accurately assess the necessary FFR capacity for maintaining frequency Nadir after disturbances, thereby facilitating the integration of higher levels of RES. Ultimately, this framework supports decarbonization efforts and ensures compliance with operational constraints by providing a practical and efficient methodology for determining FFR capacity requirements.

1.2. Literature review

Several methods have been proposed in the literature to address the FFR sizing problem. The tuning and sizing of a BESS that utilizes conventional frequency droop-based controller using a chaotic artificial bee colony scaled by fitness metaheuristic optimization under deterministic worst-case scenarios was proposed in [11]. The objective function of this study is to minimize Nadir and RoCoF after a significant event. To improve Nadir, RoCoF, and voltage deviation, in [12] a multi-objective binary gray wolf optimization approach is investigated to optimize storage system size and placement using a droop-based controller. In [13], the rated power of the BESS and the gain of a droop-based controller were selected to minimize a cost function using the BAT optimization algorithm (BOA). This optimization was subject to the constraint that the Nadir must remain below the threshold of the first stage in the Under-Frequency Load Shedding (UFLS) protection scheme. In [14], the authors aim to optimally size a BESS to provide primary frequency control, thereby maximizing the profit for the owner based on historical frequency measurement data. In [15], the metaheuristic gray wolf optimization algorithm is used to determine the size of the BESS that will provide the frequency response to minimize Nadir.

A detailed optimization methodology that utilizes a mathematical model for frequency dynamics to integrate frequency stability constraints into BESS sizing is proposed in [16]. This work focuses on microgrids and effectively addresses both grid-connected and islanded modes. This method is implemented in a small number of scenarios and does not consider UFLS, restricting its broader applicability in larger and more complex systems. In place of optimization algorithms, an inexpensive computational approach for the ESS size is proposed in [17], which estimates the system performance after a disturbance using an analytical method. In [18], simplified analytical equations are used to calculate the size of the BESS required to provide the frequency response based on a reference outage event. In [19], a step reduction iterative algorithm was investigated to dimension the BESS size that provides FFR to regulate the maximum frequency deviation after an outage. An iterative method for different BESS power levels is proposed in [20] where the optimal size is determined by two semi-empirical criteria: (1) increasing the BESS size does not provide significant improvement, and (2) based on BESS maximum discharge power efficiency.

1.3. Novelty and contributions

Unlike the continuous support provided by droop-based methods, the FFR method considered in this work operates with a discrete activation pattern, rendering most existing methodologies unsuitable for optimizing BESS sizing. Our methodology addresses this challenge by incorporating the discrete nature of FFR into the DSA framework. While state-of-the-art metaheuristic methodologies typically require numerous iterations per deterministic scenario – making them computationally prohibitive when analyzing hundreds of historical operating conditions – our gradient descent-based approach achieves convergence with significantly fewer iterations. This efficiency advantage is particularly notable when compared to exhaustive iterative methods [20] that evaluate all possible BESS sizes without optimization heuristics.

Existing approaches [11,12,15] frequently focus on general frequency response improvement rather than targeting specific Nadir thresholds, often resulting in oversized storage systems. Moreover, a critical gap persists in the computational methods for disturbance event analysis. Current methodologies relying on static equations suffer from accuracy limitations due to necessary simplifying assumptions and fail to account for crucial protection schemes like UFLS. Our proposed method addresses these limitations through full dynamic simulation that explicitly models system nonlinearities and discrete protection events.

The principal contributions of this work are:

- Quantitative characterization of the nonlinear interactions between KE, FFR, FCR, and frequency Nadir in low-inertia systems
- A novel data-driven algorithm for FFR sizing that incorporates UFLS protection schemes through dynamic security assessment
- Experimental validation using real-world operational data from the Cyprus power system, demonstrating the method's computational efficiency and practical effectiveness

This paper is structured as follows. In Section 2, a brief explanation of frequency control and relevant frequency reserve products is provided. Section 3 details the proposed framework for sizing the FFR requirements. The results are analyzed in Section 4. Finally, conclusions are drawn in Section 5.

2. Technical background

2.1. Frequency support mechanisms and products

Correction of power imbalances in power systems (and, therefore, frequency deviations) has traditionally been performed in a hierarchical manner, where each control stage is distinct from the subsequent stages. In the initial stage after a disturbance, the KE response is activated within a few milliseconds (ms), helping to maintain the initial RoCoF [21]. Following this, the FCR comes into play within a few seconds, aiming to stabilize the frequency [2]. In the third stage, the FRR is deployed with a response time of several minutes to restore the frequency to its nominal value. Finally, replacement reserves (RR) are utilized to replenish the available reserves and prepare the system for future disturbances [2,22,23]. The FRR and RR products are not relevant to the time scales investigated in this work and will therefore not be addressed.

2.1.1. Kinetic energy (KE)

In power systems, KE refers to the energy stored in large rotating generators and certain industrial motors. This stored energy is particularly valuable in situations of power imbalance [24,25]. Lower system inertia can lead to increased frequency sensitivity during disturbances, as any change in power balance has a more immediate impact on frequency due to limited KE [21]. It has been shown (see Section 2 of [10]) that KE has a direct impact on the initial RoCoF after a disturbance and a secondary, minor impact on the frequency Nadir.

2.1.2. Frequency containment reserves (FCR)

The scope of FCR[1] is to restrict the frequency of the network within predefined levels [26]. FCR is enabled within a few seconds, with full activation occurring no later than 30 s [2], and its duration can last up to 30 min, depending on the technical characteristics of the system [27]. The power contribution of FCR varies linearly with the frequency deviation up to a maximum value. It is an asymmetric product, meaning that it separately defines the upward and downward reserve needs [28]. It has been shown (see Section 2 of [10]) that FCR has a direct impact on the post-fault frequency steady state and a secondary, minor impact on the frequency Nadir.

2.1.3. Under-frequency load shedding (UFLS)

A low-frequency Nadir after a disturbance can trigger UFLS protections in the power system when the FCR is not fast enough or when the RoCoF is too high [29]. UFLS schemes stop the frequency drop after a disturbance by disconnecting feeders from the distribution system to "shed load". Various stages of UFLS are usually defined, with each stage progressively disconnecting different segments of the load. UFLS safeguards against low-frequency Nadir and minimizes the requirements for FCR. However, excessive use of UFLS leads to low reliability and significant "lost load" and is considered undesirable due to its negative socio-economic impacts. Unfortunately, low-inertia power systems experience an increase in UFLS activations [30] as low KE and FCR influence the frequency Nadir.

[1] In many countries, this product is referred to as primary frequency response.

2.2. Fast frequency response (FFR)

As the system experiences higher penetration of RES and reduced KE, the time gap between the KE response and FCR activation leads to a lower Nadir. FFR plays a pivotal role in bridging this gap and preventing UFLS activations [25,26]. FFR reacts within a very short time frame, usually in less than one second after a disturbance [25], injecting power into the grid for a short period to reduce the frequency Nadir. Although FFR complements KE and FCR, it does not reduce the minimum reserve requirements for these mechanisms and, therefore, cannot replace them [24]. Fig. 2 shows an example of how FFR affects the frequency Nadir during a generation loss event of 95 MW in a power system with a total load consumption of 825 MW, PV generation of 100 MW, and wind generation of 50 MW in a low-inertia system. This figure clearly demonstrates that FFR impacts the frequency Nadir but does not affect RoCoF or the post-fault steady-state frequency.

There are several implementations of FFR, each offering unique characteristics [31]. Some of these methodologies are presented in [1, 25]. In line with the analysis conducted by EirGrid and NEM [25], an FFR implementation that follows a step response will be used in the current work. Fig. 2 illustrates the behavior of the active power response of BESS when receiving an FFR activation signal. A local frequency measurement unit detects the frequency level, and when it drops below a certain threshold (usually 49.7 Hz), the local controller immediately injects the maximum FFR power. Subsequently, the support duration lasts for 30 s. Finally, the deactivation process takes approximately 20 s, during which power is reduced at a constant rate, allowing sufficient time for the system's dynamics to stabilize the frequency without causing abrupt changes in power.

2.3. Interaction between KE, FFR, FCR and Nadir

Three critical frequency stability indicators must be analyzed following disturbances in low-inertia systems: RoCoF, post-fault steady-state frequency, and frequency Nadir. Excessive RoCoF risks triggering generator protections and cascading outages, while a depressed Nadir may violate Frequency Ride-Through (FRT) requirements or activate UFLS. Prolonged low steady-state frequencies can disrupt synchronized operations and lead to sustained outages.

The initial RoCoF derives from system inertia and power imbalance through the linear relationship (1) while steady-state frequency deviation $\Delta f_{\max}$ depends on the combined regulation from generators and loads as shown in (2).

$$\text{RoCoF} = \frac{\Delta P \cdot \omega_n}{2H} \tag{1}$$

$$\Delta f_{\max} = \frac{\Delta P}{L_R + G_R} \tag{2}$$

where ΔP represents the power imbalance, ω_n the nominal angular frequency, H the total system inertia constant, L_R the load self-regulation coefficient, and G_R the generator frequency containment reserve capacity. These linear relationships enable straightforward inertia and FCR requirement calculations [32].

However, the influence of KE and FCR on the frequency Nadir following a significant event exhibits a strongly non-linear relationship, incorporating KE, FCR response time, and FCR capacity [6]. A dynamic assessment of the Cyprus power system, shown in Fig. 3, demonstrates the impact of these factors under various scenarios. The scenarios, representing one year of historical operating points and filtered for the most critical conditions (e.g., largest post-fault imbalance power),

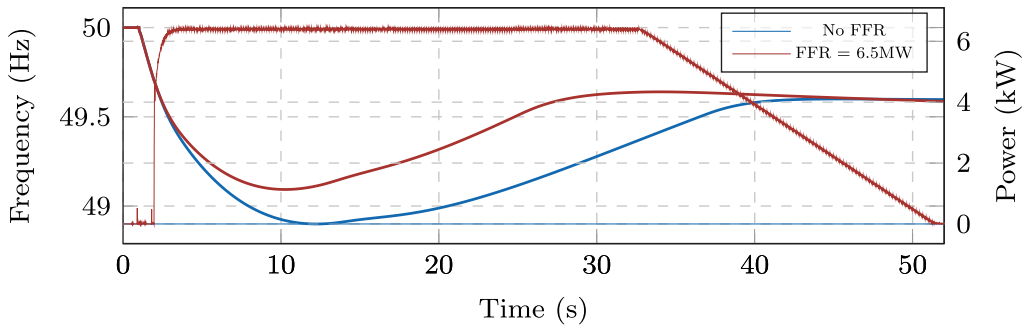

Fig. 2. Loss of generator event ($\Delta P = 95$ MW), frequency response and corresponding FFR active power response.

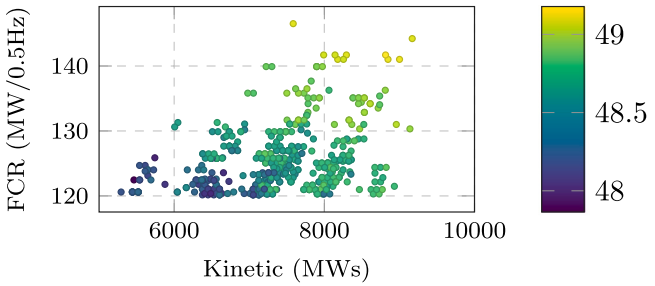

Fig. 3. Post-disturbance frequency Nadir (color scale) as a function of KE (x-axis) and FCR (y-axis). Warmer colors indicate safer Nadir > 49 Hz. (For interpretation of the references to color in this figure legend, the reader is referred to the web version of this article.)

include total load consumption ranging from 350 MW to 1200 MW and RES generation varying between 11 MW and 415 MW (installed capacity: 765 MW).

Fig. 3 reveals a general trend: higher KE and FCR levels lead to improved Nadir (warmer colors). However, some inconsistencies are apparent—scenarios with lower KE and FCR occasionally produce higher Nadir values due to the faster response times of FCR-providing units. This emphasizes the importance of FCR activation speed alongside capacity. In summary, higher KE and larger FCR capacity improve Nadir values. Crucially, faster FCR response times further enhance results, highlighting their role in mitigating frequency issues.

To ensure the frequency security, the Cyprus TSO must maintain Nadir values above 49 Hz. In Fig. 4a, critical historical operating points exhibit frequency drops below this threshold (red). FFR, with rapid activation, can address this issue by mitigating low-frequency Nadir problems independently of KE and FCR capacity. Figs. 4b and 4c illustrate the impact of incorporating 10 MW and 20 MW of FFR, respectively, reducing frequency violations and increasing system resilience.

3. Methodology

This section presents the proposed data-driven approach for determining the optimal BESS size for FFR operation, summarized in Fig. 5. The algorithm iteratively computes the required FFR capacity to achieve a frequency Nadir close to the target value (f^{tgt}_{Nadir}). It integrates DSA to calculate the deviation of the Nadir from f^{tgt}_{Nadir} and employs a gradient descent-based linear prediction method to estimate the necessary FFR reserves in each iteration, as detailed in the flowchart in Fig. 6.

Initially, historical operating points are filtered to retain only the most critical scenarios. In the first iteration, FFR is set to zero, and dynamic simulations are performed for all scenarios, considering an outage of the largest infeed generator. Scenarios where the frequency Nadir violates the threshold are retained, and the FFR estimator uses the dynamic response to predict the required FFR to bring the Nadir closer to the target value. The process repeats until convergence.

The following subsections provide a detailed analysis of the methodology.

3.1. Scenario selection

The proposed data-driven approach utilizes historical operational data to size FFR. To reduce computational complexity, a filtering process is applied to retain only the most critical operating scenarios. Specifically, the filter selects scenarios where the largest generator (highest infeed) operates at the top 1% of its maximum power output across the entire dataset. These scenarios represent the most severe conditions for frequency stability.

3.2. Error estimation based on dynamic security assessment (DSA)

For the selected scenarios, a DSA is conducted, assuming the disconnection of the largest infeed in each case. The DSA uses non-linear dynamic models of power system components to simulate the disturbance event and capture the corresponding frequency dynamics. Each scenario is simulated over 60 s to extract key post-disturbance metrics, including frequency Nadir, RoCoF, post-fault steady-state frequency, and FCR activation timing.

Initially, the FFR power is set to zero ($P^{max}_{FFR,0} = 0$) for the first DSA computation. The process is embarrassingly parallel for each scenario, allowing simulations to be accelerated using multicore computing. Once the DSA simulations are complete, scenarios where the frequency Nadir falls below the target ($f_{\text{Nadir}} < f^{\text{tgt}}_{\text{Nadir}}$) or where the existing FFR causes the Nadir to overshoot the target ($f_{\text{Nadir}} \geq 1.01 \cdot f^{\text{tgt}}_{\text{Nadir}}$) are retained. These represent cases where insufficient or excessive FFR is applied, respectively, ensuring that the methodology focuses on scenarios requiring adjustment.

3.3. FFR estimation based on linear prediction

For scenarios that violate the requirements defined in the previous paragraph, the estimated FFR needs are calculated using the FFR linear estimator in Algorithm 1. After the process is completed, we extract the minimum and maximum FFR requirements for all the scenarios analyzed and iterate. There are two options in the proposed estimator for calculating the FFR power (P^{max}_{FFR}) in Algorithm 1. In the first case, activation of UFLS is not allowed – thus, we assume that the f^{tgt}_{Nadir} is higher than the first setpoint of activation of UFLS ($f^{tgt}_{Nadir} \geq f_{UFLS,1}$). In the second case, the activation of one level of UFLS is allowed. This option provides a compromise between reliability and investment costs for FFR.

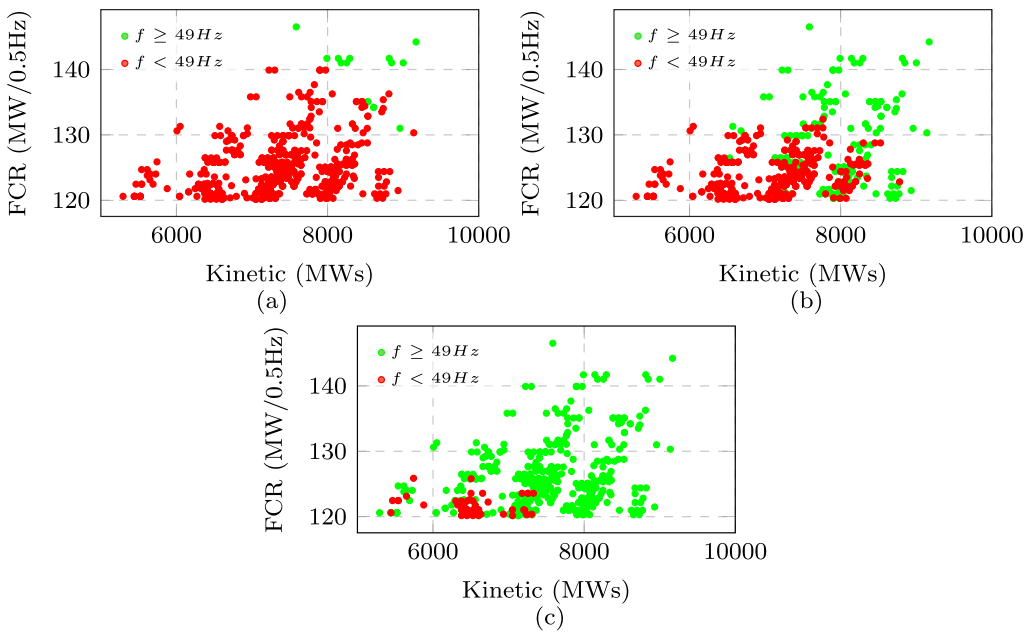

Fig. 4. Post-disturbance frequency Nadir as a function of KE, FCR, and FFR Active Power (a) 0MW, (b) 10MW and (c) 20MW. (For interpretation of the references to color in this figure legend, the reader is referred to the web version of this article.)

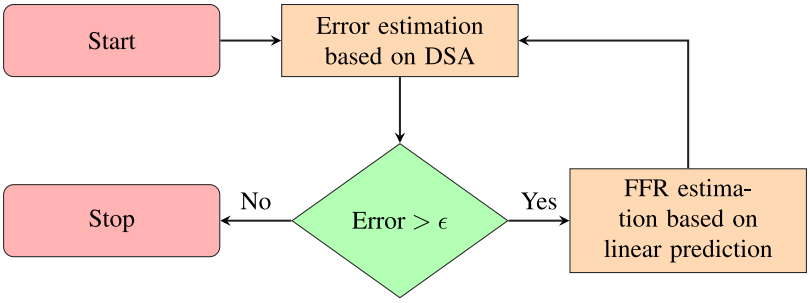

Fig. 5. Simplify flowchart of the proposed iterative methodology.

Algorithm 1: FFR estimator at each iteration of algorithm at Fig. 6

Data: Filtered scenarios
Result: FFR requirements ($P^{max}_{FFR,i}$) for each scenario
if *avoiding UFLS* **then**
  Calculate $P^{max}_{FFR,i}$ based on (3);
else if *allowing 1st level UFLS* **then**
  Calculate $P^{max}_{FFR,i}$ based on (5);

3.3.1. FFR estimation based on linear prediction without UFLS activation

The following equations are used to estimate the required FFR values ($P^{max}_{FFR,i}$) for the ith ($i > 0$) iteration:

$$\Delta P^{mean}_{FFR,i} = \Delta P^{max} - \frac{f^{start}_{FFR} - f^{tgt}_{Nadir}}{t^{Nadir}_{i-1} - t^{start}_{i-1,FFR}} \cdot 2 \cdot \frac{KE}{f_N} - P^{mean}_{FFR,i-1} - P^{mean}_{LR} - P^{mean}_{FCR,i-1} \tag{3a}$$

$$P^{max}_{FFR,i} = \Delta P^{mean}_{FFR,i} \cdot \frac{t^{Nadir}_{i-1} - t^{start}_{i-1,FFR}}{t^{Nadir}_{i-1} - t^{start}_{i-1,FFR} - \frac{T^{max}_{FFR}}{2}} + P^{max}_{FFR,i-1} \tag{3b}$$

where:

KE is the available kinetic during the disturbance event,
f_N is the nominal frequency,
f^{start}_{FFR} is the FFR activation frequency,
$t^{start}_{i-1,FFR}$ is the FFR activation time based on previous iteration,
$P^{mean}_{FCR,i-1}$ is the average FCR of the previous iteration,
P^{mean}_{LR} is the average load self-regulation calculated using (4),
$P^{mean}_{FFR,i-1}$ is the FFR average power of the previous iteration from the FFR activation point to UFLS,
T^{max}_{FFR} is the time that the unit needs to take the peak value from the time of activation,
t^{Nadir}_{i-1} is the Nadir time of the previous iteration,
ΔP^{max} is the power deviation of the disturbance event.

Eq. (3a) uses a linear estimation approach, depicted in Fig. 7a with the blue line, to estimate the required $P^{max}_{FFR,i}$ based on Dynamic Security Assessment (DSA) results. The black line shows the actual frequency response from the previous iteration, while the green line represents the updated response after incorporating the computed FFR in the dynamic model.

The linear estimator is inspired by the swing equation, which relates the RoCoF to the power imbalance (ΔP) as $RoCoF = \Delta P \cdot \frac{\omega_n}{2 \cdot H_{sys}}$. Here, ΔP evolves over time, modified by FFR, FCR power injections, and load self-regulation, represented as a mean value in (3a). An increase in kinetic energy or FCR capacity reduces the negative terms (KE and $P^{mean}_{FCR,i-1}$), thereby decreasing the FFR requirement. In critical scenarios, as the time difference between the frequency Nadir and FFR activation ($t_{Nadir} - t_{start}$) increases, the denominator grows, requiring more FFR

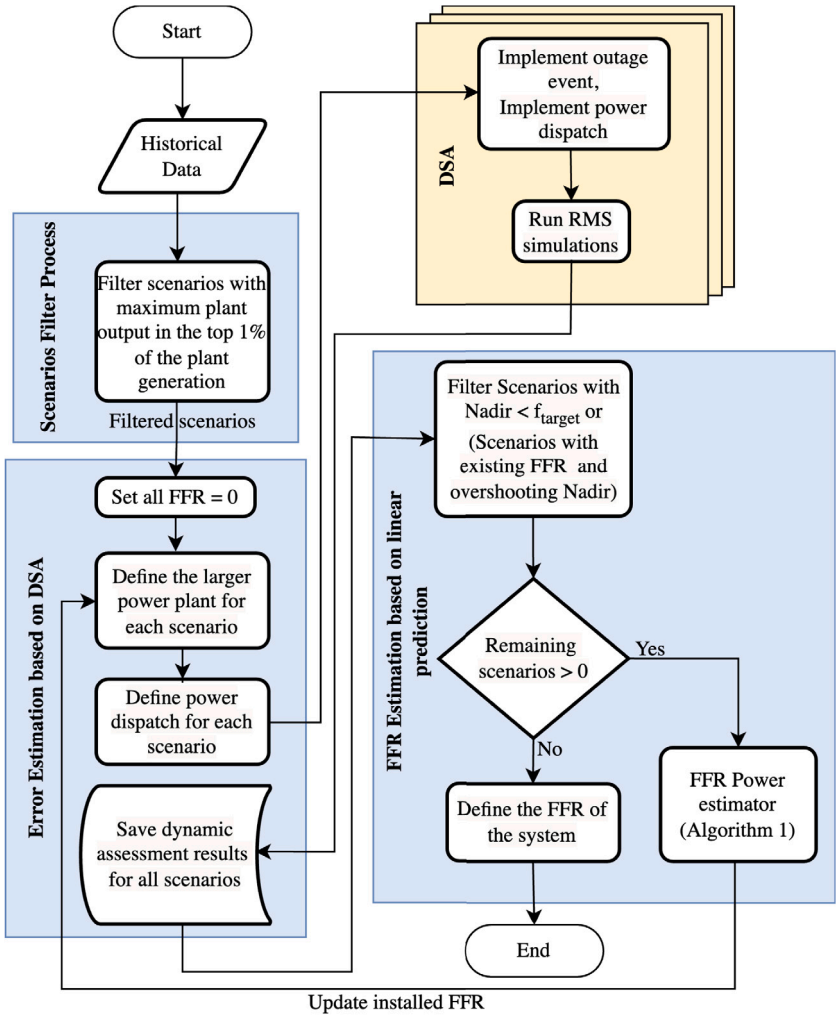

Fig. 6. Flowchart of proposed methodology for FFR sizing.

power. Conversely, lowering the targeted Nadir (f_{tgt}) or activating FFR earlier (t_{Nadir}) reduces the FFR requirements by affecting the numerator ($f_{start} - f_{tgt}$). These dynamics make FFR sizing sensitive to Nadir targets, activation times, and system conditions.

Eq. (3b), derived from Fig. 7b, converts the mean estimated FFR power (P_{FFR}^{mean}) into the maximum value (P_{FFR}^{max}) used for FFR sizing. In this context, the mean value is calculated as the sum of areas A1, A2, and A3 divided by their corresponding time intervals. A1 represents the FFR activation time, A2 the time to reach UFLS activation, and A3 the time to reach the Nadir.

The mean load self-regulation power (P_{LR}^{mean}) accounts for the natural change in load power during the event, which occurs as a response to frequency variations and contributes to system stability [33]. It is computed between the FFR activation and the targeted frequency using Eq. (4):

$$P_{LR}^{mean} = k \cdot P_{load}^{total} \cdot \frac{(f_N - f_{FFR}^{start}) + (f_N - f_{Nadir}^{tgt})}{2} \tag{4}$$

where k is the load self-regulation coefficient, and P_{load}^{total} is the total load demand prior to the disturbance.

3.3.2. FFR estimation based on linear prediction with first-stage UFLS activation

In some cases, allowing the activation of the first UFLS stage can significantly reduce the required FFR capacity without compromising the secure operation of the system. In this case, the following equations are used to estimate the required FFR values ($P_{FFR,i}^{max}$) for the ith iteration ($i > 0$):

$$\frac{f_{FFR}^{start} - f_{UFLS}^{1st}}{t_{i-1,UFLS}^{1st} - t_{i-1,FFR}^{start}} = \frac{f_N}{2 \cdot KE} \cdot (\Delta P^{max} - P_{FFR,i-1,a}^{mean} - P_{LR,a}^{mean} - P_{FCR,i-1,a}^{mean} - \Delta P_{FFR,a}^{mean}) \tag{5a}$$

$$\frac{f_{UFLS}^{1st} - f_{Nadir}^{tgt}}{t_{i-1}^{Nadir} - t_{i-1,UFLS}^{1st}} = \frac{f_N}{2 \cdot KE} \cdot (\Delta P^{max} - P_{FFR,i-1,b}^{mean} - P_{LR,b}^{mean} - P_{FCR,i-1,b}^{mean} - P_{UFLS}^{1st} - \Delta P_{FFR,b}^{mean}) \tag{5b}$$

$$P_{LR,a}^{mean} = k \cdot P_{load}^{total} \cdot \frac{(2 \cdot f_N - f_{FFR}^{start} - f_{UFLS}^{1st})}{2} \tag{6a}$$

$$P_{LR,b}^{mean} = k \cdot P_{load}^{total} \cdot \frac{(2 \cdot f_N - f_{UFLS}^{1st} - f_{Nadir}^{tgt})}{2} \tag{6b}$$

$$P_{UFLS}^{1st} = LD_{shed}^{\%,1st} \cdot P_{load}^{total} - PV_{shed}^{\%,1st} \cdot P_{PV}^{total} \tag{6c}$$

$$\Delta P_{FFR,a}^{mean} = \frac{(t_{i-1,UFLS}^{1st} - t_{i-1,FFR}^{start} - \frac{T_{FFR}^{max}}{2})}{t_{i-1,UFLS}^{1st} - t_{i-1,FFR}^{start}} \cdot \Delta P_{i,FFR}^{max} \tag{6d}$$

$$\Delta P_{FFR,b}^{mean} = \Delta P_{i,FFR}^{max} \tag{6e}$$

$$P_{FFR,i}^{max} = P_{FFR,i-1}^{max} + \Delta P_{i,FFR}^{max} \tag{6f}$$

where:

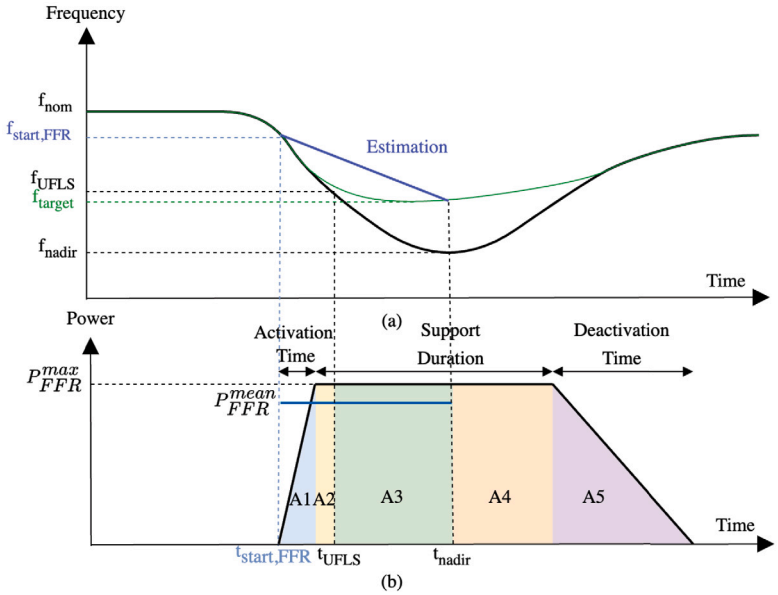

Fig. 7. (a) Post-disturbance frequency response (black is the simulated response without FFR, green is the target response with the FFR, blue is the linear estimator), (b) BESS FFR active power response.

f^{1st}_{UFLS} is the frequency at which the first UFLS stage activates,

$t^{1st}_{i-1,UFLS}$ is the time at which the first UFLS stage of the previous iteration activated,

$P^{mean}_{FFR,i-1,a/b}$ is the FFR average power of the previous iteration where a corresponds to the time from FFR activation until the first UFLS stage, and b corresponds to the time from the first UFLS stage activation until the f^{tgt}_{Nadir} value.

$P^{mean}_{LR,a/b}$ is the average load self-regulation where a corresponds from the FFR activation time until the first UFLS stage activation and b corresponds from the first UFLS stage activation time until the f^{tgt}_{Nadir}. Calculated using (6a) and (6b) respectively,

$P^{mean}_{FCR,i-1,a/b}$ is the FCR average power of the previous iteration where a corresponds to the time from FFR activation until the first UFLS stage, and b corresponds to the time from the first UFLS stage activation until the f^{tgt}_{Nadir} value,

P^{1st}_{UFLS} is the net power disconnected considering the first-stage UFLS activation.

Eqs. (5) use the same estimation approach as (3a) but divide the operation into two time segments. In the first segment, (5a) describes the frequency response before the first UFLS activation, and in the second segment, (5b) describes the frequency response from the moment UFLS is activated until the Nadir. This segmentation is necessary due to the discrete nature of UFLS protection. As mentioned above, the ΔP of the system varies during the event. When UFLS activation occurs, there is a significant reduction in the power imbalance. Therefore, segmentation is mandatory and helps improve the accuracy of the solution.

To define the maximum FFR power in each iteration ($P^{max}_{FFR,i}$), (5) is solved for $P^{max}_{FFR,i}$. When more than one UFLS stage is accepted, (5) can be modified accordingly by dividing it into additional time segments.

3.4. BESS power and energy sizing

After the iterative method converges (when there are no pending scenarios) or the maximum number of iterations is reached, the FFR requirement is determined as the maximum value across all analyzed scenarios (infinite norm). Thus, the BESS power capacity must at least match this value to ensure compliance with FFR requirements. The energy capacity of the BESS is then computed based on the maximum power requirement by integrating the power response over time, equivalent to calculating the area under the curve shown in Fig. 7b.

The energy requirement is calculated by dividing the response curve into segments (A1, A2, A3, A4, and A5) and summing the integrals of each. These integrals represent the energy contribution during the activation, support, and deactivation stages. For example, given the activation time (T_{act}), deactivation time (T_{deact}), support duration (T_{supp}), and the maximum FFR power (P^{max}_{FFR}), assuming linear activation and deactivation as shown in Fig. 7b, the total energy requirement can be calculated as follows:

$$E = P^{max}_{FFR} \cdot \frac{\left(\frac{T_{act}+T_{deact}}{2} + T_{supp}\right)}{3600} \tag{7}$$

4. Experimental results

In this section, the proposed algorithm was tested on the Cyprus power system, the diagram of which is shown in Fig. 8, to validate the methodology. The results are presented for two cases: one where no stage of UFLS is permitted and another where a single stage of UFLS is accepted.

The Cyprus power system consists of 26 conventional SG-based plants (steam, gas, and diesel). All generators are modeled with Automatic Voltage Regulators (AVR), Governors (GOV), and Power System Stabilizers (PSS), as detailed by the TSO of Cyprus, ensuring an accurate representation of their dynamic behavior. Additionally, the system includes 155 MW of wind farms and 610 MW of distributed PV generation. Historical load data indicate a minimum demand of 300 MW and a peak of approximately 1240 MW.

This model, used by the TSO of Cyprus for operational and planning studies related to frequency services, includes a reduced network model while maintaining detailed dynamic models for generators, loads, and RES components. It is implemented in DIgSILENT PowerFactory and incorporates UFLS protection schemes and an aggregated BESS with the FFR implementation described in Section 2.2.

4.1. System parameters and scenario selection

The generator capacities for conventional plants are given in Table 1. The minimum KE was calculated to keep the RoCoF within the

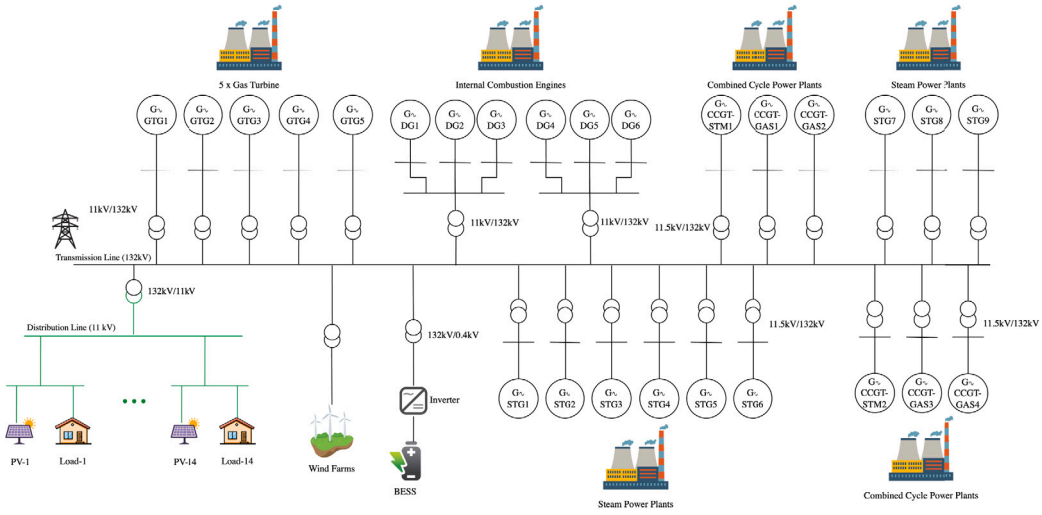

Fig. 8. One-line diagram of the simplified Cyprus system.

Table 1
Maximum generator active power dispatch.

Generator	Max power (MW)
GTG1-GTG5	20
DG1-DG6	15
CCGT-STM1	35
CCGT-STM2	35
GAS1-GAS4	45
STG1-STG6	45
STG7	120
STG 8–9	105

Table 2
First UFLS levels in the Cyprus system.

Stage	Frequency	$PV_{\%}^{shed}/LD_{\%}^{shed}$
1	49	4%
2	48.9	4%
3	48.8	3%

Table 3
Test system parameters [8,34].

Parameter	Value
k	1%
Minimum KE	3000 MWs
Minimum FCR	120 MW
Freq. at normal operation	49.8–50.2 Hz
Freq. during disturbance	47–52 Hz
Post-fault freq. steady state	49.5–50.5 Hz
ΔP	120 MW
f_{Nadir}^{tgt}	48.9 & 49 Hz

required limit of $RoCoF_{max} = 1$ Hz/s. The first three stages of the UFLS protection scheme implemented in Cyprus are provided in Table 2. It should be noted that, due to the distributed nature of PVs in the system, load shedding also results in the disconnection of PV generation. Table 3 defines all the simulated parameters considered.

Based on historical operational data from the Cyprus TSO, 500 critical scenarios were selected for FFR sizing analysis. These scenarios, compliant with minimum KE and FCR thresholds, featured load consumption ranging from 300 MW to 1200 MW under maximum generation output conditions ($\Delta P = 120$ MW). Each scenario simulated the disconnection of the largest generator at $t = 1$ s through a dynamic security assessment.

The scenarios were classified into three operational regimes: *Low* denoting minimal RES, FCR, and KE levels; *Medium* reflecting balanced conventional-renewable operation; and *High* representing peak RES generation with ample reserves. Parameter ranges for these categories are detailed in Table 4, while Fig. 9 illustrates their distribution through a heatmap visualization.

4.2. Case I:

FFR sizing results without UFLS activation

In this analysis, the FFR sizing method does not allow for UFLS activation, so the frequency target was set to $f_{Nadir}^{tgt} = 49$ Hz. During the first iteration of the algorithm (with FFR initialized at zero), the DSA identified that 485 scenarios violated this requirement. Fig. 10a graphically illustrates the results of the first iteration. Then, the linear prediction of the FFR capacity is performed using (3a). Table 5 shows the evolution of the algorithm, which converges in four iterations. It should be noted that the majority of the violating scenarios in iterations 2–4 involve overshooting (i.e., the FFR calculated for these scenarios led to frequency Nadirs significantly higher than f_{Nadir}^{tgt}). The infinite norm over the required FFR for all scenarios is 33 MW. As mentioned above, the energy consumption during FFR support is very small compared to the power due to the low supply duration, with an average consumption of 0.18 MWh.

Based on the results, the correlation between the initial frequency Nadir (Nadir value before FFR implementation) and the required FFR power is shown in Fig. 10b for all scenarios. It is evident that there is an almost linear correlation between the two. By examining this figure alongside Fig. 3, we can further demonstrate the sensitivity of the methodology's output to variations in available KE and FCR within the system, underscoring how these parameters collectively influence FFR requirements. However, due to the non-linear correlation between KE and FCR with the Nadir, which arises from the varying FCR response times, direct estimation of FFR solely from KE and FCR is not possible. This highlights the need for a more detailed assessment incorporating response dynamics to improve predictive capability.

Furthermore, the correlation shown in Fig. 10c between the initial RoCoF (RoCoF before FFR implementation) and FFR power requirements reveals a notable trend: as RoCoF decreases, there is a corresponding increase in FFR requirements. However, due to the varying FCR response times and FCR capacities across scenarios – factors independent of RoCoF – a significant dispersion exists, making it difficult to establish a clear correlation.

Table 4
Categorization of scenarios based on RES, FCR, and KE ranges.

Category	RES generation (MW)	FCR capacity (MW)	Kinetic energy (MWs)
Low	10–165	120–122	5335–7130
Medium	165–260	122–126	7130–7694
High	260–415	126–151	7694–9228

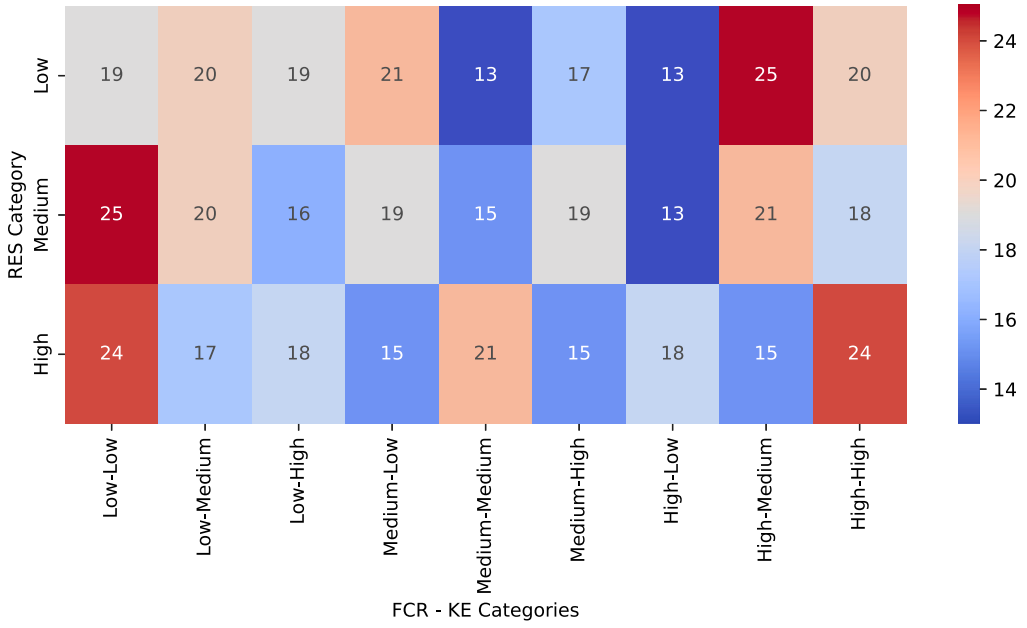

Fig. 9. Scenario distribution across RES, FCR, and KE categories, with the color scale indicating the number of scenarios in each category combination. (For interpretation of the references to color in this figure legend, the reader is referred to the web version of this article.)

Table 5
Results without UFLS activation.

Iteration	No. of scenarios		FFR (MW)		Nadir (Hz)		Energy (MWh)
	Analyzed	Violating	Min	Max	Min	Max	Average
1	500	485	0	0	47.69	49.27	0
2	485	416	4.9	33	49.04	49.17	0.25
3	416	29	3.9	26.5	49.01	49.12	0.17
4	29	0	4.9	19.2	49.1	49.12	0.12
Total	500	–	0	33	49.04	49.27	0.18

Table 6
Results with first stage of UFLS accepted.

Iteration	No. of scenarios		FFR		Nadir		Energy (MWh)
	Analyzed	Violating	Min	Max	Min	Max	Average
1	500	105	0	0	48.61	49.27	0
2	105	0	10	19	48.95	48.98	0.14
Total	500	0	0	18.75	48.95	49.27	0.03

4.3. Case II:

FFR sizing results with first stage of UFLS

The analysis permits activation of the first Under-Frequency Load Shedding (UFLS) stage, with target frequency $f^{tgt}_{Nadir} = 48.9$ Hz (threshold for second-stage UFLS activation). Initial Dynamic Security Assessment (DSA) with zero FFR allocation identified 105 critical scenarios violating this threshold, as shown in Fig. 11a. Following FFR capacity prediction using (5), the algorithm converged within two iterations (Table 6).

The worst-case FFR requirement reached 18.75 MW ($\mathcal{L}_\infty$-norm), with energy consumption averaging 0.14 MWh for critical scenarios and aggregate consumption remaining at 0.03 MWh when considering all 500 operational cases. This demonstrates efficient FFR allocation where most scenarios required no reserve activation.

Fig. 11b illustrates the correlation between Nadir and the required FFR power to achieve the target. Compared to the non-UFLS case, there is slightly greater dispersion but a similar near-linear relationship. The sensitivity of the methodology to KE and FCR variations persists, but UFLS activation introduces additional complexity. The frequency trajectory is now influenced by KE, FCR, and UFLS response, making FFR estimation less predictable than in the non-UFLS scenario. Notably, no correlation between RoCoF and FFR is observed, attributable to varying FCR characteristics and the hybrid discrete-continuous dynamics introduced by UFLS.

4.4. Discussions

The methodology was evaluated under two scenarios: without UFLS and with one UFLS stage permitted. Allowing a single UFLS stage

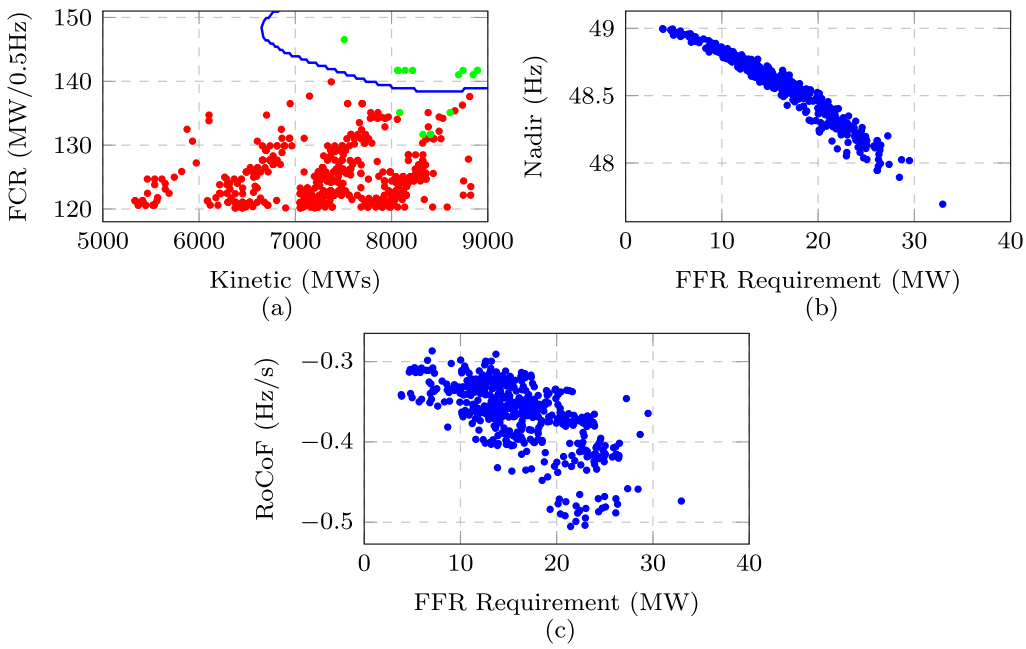

Fig. 10. Loss of generator events without activation of the UFLS scheme: (a) Nadir correlation with FCR and KE; (b) FFR requirements correlation with each scenario Nadir; and, (c) FFR requirements correlation with each scenario RoCoF.

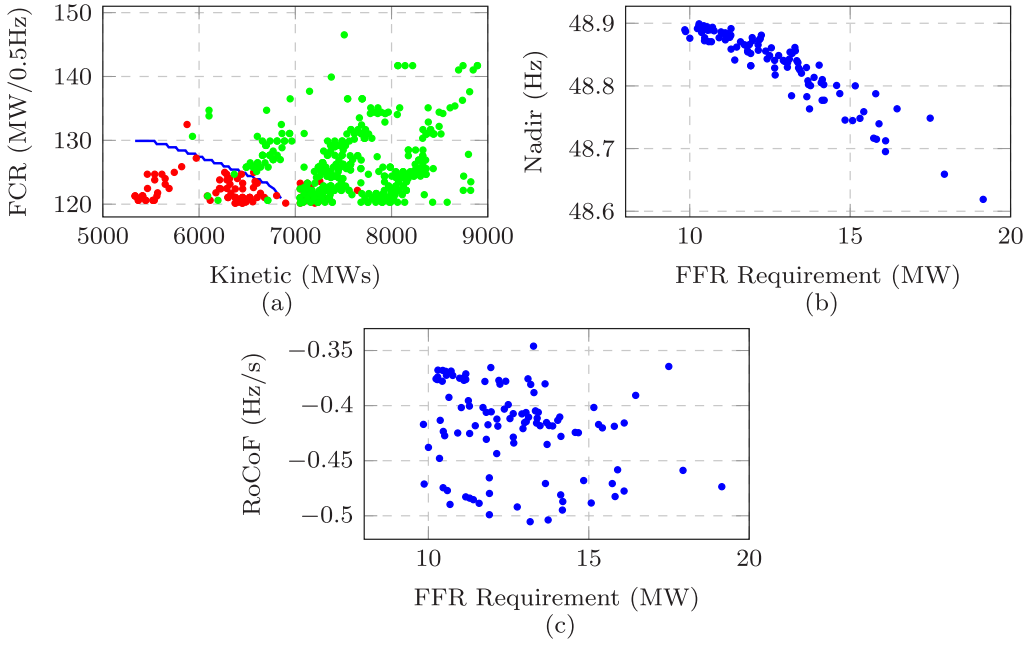

Fig. 11. Loss of generator events with the first stage of UFLS Scheme accepted. (a) Nadir correlation with FCR and KE. (b) FFR requirements correlation with each scenario Nadir. (c) FFR requirements correlation with each scenario RoCoF.

reduced maximum FFR requirements by approximately 55%. Accuracy, measured as deviation from target frequency, improved significantly with UFLS activation. As illustrated in Fig. 12, the maximum deviation decreased from 0.12 Hz (no UFLS) to 0.08 Hz (with UFLS). This enhancement likely stems from the time segmentation approach employed in the methodology.

The proposed methodology exhibits two principal limitations. First, parameter selection – particularly error tolerance, target frequency thresholds, and scenario quantity – requires careful calibration between computational efficiency and precision. Excessively tight tolerances risk non-convergence, while overly lenient settings induce conservative overdesign through excessive FFR allocations. Second, the discrete FFR activation logic coupled with full nonlinear system dynamics creates a mixed-integer differential–algebraic formulation. This mathematical complexity, involving gradient-descent minimization across numerous scenarios, fundamentally obstructs formal convergence proofs despite the method's demonstrated empirical effectiveness in practical applications.

5. Conclusion

This paper presents a novel data-driven methodology for sizing FFR requirements in low-inertia power systems, specifically addressing post-disturbance frequency Nadir security challenges. As modern grids

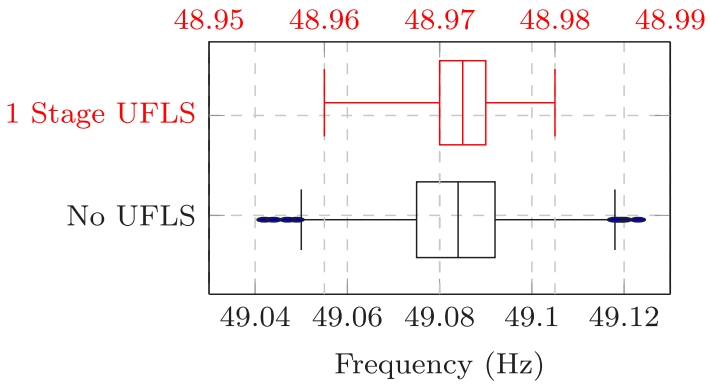

Fig. 12. Range of frequency Nadir after the implementation of the methodology.

integrate increasing levels of RES, traditional frequency support mechanisms prove inadequate, necessitating advanced solutions employing rapid-acting reserves like FFR. Through a rigorous framework combining dynamic security assessment with gradient-descent-based linear prediction, this work establishes an iterative process to optimize FFR capacity across critical historical operating scenarios.

Validation on the Cyprus power system demonstrates the method's effectiveness in enhancing grid resilience, achieving target frequency Nadir thresholds with minimal computational load while significantly reducing dependence on UFLS activations. The proposed approach exhibits strong scalability, enabling adaptation to diverse grid configurations and operational conditions without requiring fundamental algorithmic modifications. By systematically optimizing FFR allocation, the methodology reduces reliance on conventional frequency reserves while maintaining compliance with operational constraints – a critical capability for TSOs navigating the transition to high-renewable penetration scenarios.

The practical implementation framework enables TSOs to precisely determine FFR requirements for maintaining frequency security following major disturbances. This capability supports the integration of higher RES shares while preserving frequency stability, directly contributing to power sector decarbonization objectives. Strategic deployment of this methodology could prevent unnecessary conventional reserve capacity in systems comparable to Cyprus' scale, representing significant cost savings and accelerated clean energy adoption.

Future research directions will investigate three key extensions: (1) hybrid energy storage architectures integrating flywheels, synchronous condensers, and supercapacitors with BESS, (2) combined optimization of FFR placement with synthetic inertia provision strategies, and (3) stochastic formulations addressing real-time renewable variability. Additional work will develop techno-economic models balancing capital investments against reliability metrics, while advanced convex relaxation techniques will enhance computational efficiency for large-scale implementations. These developments aim to create a comprehensive decision-support toolkit for next-generation low-inertia grid operations.

CRediT authorship contribution statement

Savvas Panagi: Writing – original draft, Visualization, Software, Methodology, Investigation, Data curation. **Petros Aristidou:** Writing – review & editing, Validation, Supervision, Methodology, Funding acquisition.

Declaration of competing interest

The authors declare the following financial interests/personal relationships which may be considered as potential competing interests: Savvas Panagi reports financial support was provided by Electricity Authority of Cyprus. If there are other authors, they declare that they have no known competing financial interests or personal relationships that could have appeared to influence the work reported in this paper

Acknowledgments

The authors would like to thank Cyprus TSO for providing the dynamic model and operational data used to validate the proposed dimension methodology. This project has received funding from the European Union's Horizon Europe Framework Program (HORIZON) under the GA n. 101120278 - DENSE.

Data availability

The data that has been used is confidential.

References

[1] ENTSOE, Future System Inertia 2, Tech. Rep., 2017, URL https://eepublicdownloads.entsoe.eu.
[2] ENTSOE, Operational Reserve Ad Hoc Team Report, Tech. Rep., 2012, URL https://eepublicdownloads.entsoe.eu.
[3] Z.A. Obaid, L.M. Cipcigan, L. Abrahim, M.T. Muhssin, Frequency control of future power systems: reviewing and evaluating challenges and new control methods, J. Mod. Power Syst. Clean Energy 7 (1) (2019) 9–25, http://dx.doi.org/10.1007/s40565-018-0441-1.
[4] Paris Agreement, United Nations, 2018.
[5] B.J. Kirby, J. Dyer, C. Martinez, R.A. Shoureshi, R. Guttromson, J. Dagle, et al., Frequency Control Concerns in the North American Electric Power System, United States. Department of Energy, 2003.
[6] M. Rezkalla, M. Pertl, M. Marinelli, Electric power system inertia: requirements, challenges and solutions, Springer 42 (3) (2018) 2677–2693, http://dx.doi.org/10.1007/s00202-018-0739-z.
[7] Fingrid, fast frequency reserve, 2025, URL https://www.fingrid.fi. (Accessed: 05 February 2025).
[8] Transmission System Operator of Cyprus, Cyprus Transmission Code 1.1.0, 2023.
[9] AEMO, Fast frequency response (FFR), 2023, URL https://visualisations.aemo.com.au.
[10] U. Markovic, Z. Chu, P. Aristidou, G. Hug, LQR-based adaptive virtual synchronous machine for power systems with high inverter penetration, IEEE Trans. Sustain. Energy (ISSN: 1949-3029) 10 (3) (2019) 1501–1512, http://dx.doi.org/10.1109/TSTE.2018.2887147.
[11] C.K. Das, T.S. Mahmoud, O. Bass, S. Muyeen, G. Kothapalli, A. Baniasadi, N. Mousavi, Optimal sizing of a utility-scale energy storage system in transmission networks to improve frequency response, J. Energy Storage 29 (2020) 101315.
[12] A.F. Ramos, I. Ahmad, D. Habibi, T.S. Mahmoud, Placement and sizing of utility-size battery energy storage systems to improve the stability of weak grids, Int. J. Electr. Power Energy Syst. 144 (2023) 108427.
[13] M. Ramírez, R. Castellanos, G. Calderón, O. Malik, Placement and sizing of battery energy storage for primary frequency control in an isolated section of the mexican power system, Electr. Power Syst. Res. 160 (2018) 142–150.
[14] A. Oudalov, D. Chartouni, C. Ohler, Optimizing a battery energy storage system for primary frequency control, IEEE Trans. Power Syst. 22 (3) (2007) 1259–1266, http://dx.doi.org/10.1109/TPWRS.2007.901459.

[15] K.S. El-Bidairi, H.D. Nguyen, T.S. Mahmoud, S. Jayasinghe, J.M. Guerrero, Optimal sizing of battery energy storage systems for dynamic frequency control in an islanded microgrid: A case study of Flinders Island, Australia, Energy 195 (2020) 117059.

[16] M. Javadi, Y. Gong, C. Chung, Frequency stability constrained BESS sizing model for microgrids, IEEE Trans. Power Syst. 39 (2) (2023) 2866–2878.

[17] D. Pandit, N. Nguyen, J. Mitra, An analytical approach to energy storage sizing for inertia and frequency reserve support, in: 2022 IEEE Power and Energy Society General Meeting, PESGM, 2022, pp. 1–5, http://dx.doi.org/10.1109/PESGM48719.2022.9917159.

[18] V. Knap, S.K. Chaudhary, D.-I. Stroe, M. Swierczynski, B.-I. Craciun, R. Teodorescu, Sizing of an energy storage system for grid inertial response and primary frequency reserve, IEEE Trans. Power Syst. 31 (5) (2016) 3447–3456, http://dx.doi.org/10.1109/TPWRS.2015.2503565.

[19] U. Akram, N. Mithulananthan, R. Shah, S. Alzahrani, Design of energy storage for frequency stability in low-inertia power grid, IEEE Syst. J. 17 (3) (2023) 4763–4774, http://dx.doi.org/10.1109/JSYST.2023.3280163.

[20] H. Alsharif, M. Jalili, K.N. Hasan, Power system frequency stability using optimal sizing and placement of battery energy storage system under uncertainty, J. Energy Storage 50 (2022) 104610.

[21] ENTSOE, Requirement for Minimum Inertia in the Nordic Power System, Tech. Rep., 2021.

[22] M. Caprabianca, M.C. Falvo, L. Papi, L. Promutico, V. Rossetti, F. Quaglia, Replacement reserve for the italian power system and electricity market, Energies 13 (11) (2020) 2916.

[23] R. Hollinger, A.M. Cortes, T. Erge, Fast frequency response with BESS: A comparative analysis of Germany, great britain and Sweden, in: 2018 15th International Conference on the European Energy Market, EEM, 2018, pp. 1–6, http://dx.doi.org/10.1109/EEM.2018.8469998.

[24] ENTSOE, Fast Frequency Reserve – Solution to the Nordic inertia challenge, Tech. Rep., 2019, URL https://eepublicdownloads.entsoe.eu.

[25] L. Meng, J. Zafar, S.K. Khadem, A. Collinson, K.C. Murchie, F. Coffele, G.M. Burt, Fast frequency response from energy storage systems—A review of grid standards, projects and technical issues, IEEE Trans. Smart Grid 11 (2) (2020) 1566–1581, http://dx.doi.org/10.1109/TSG.2019.2940173.

[26] N. Modig, R. Eriksso, P. Ruokolainen, J. Ødegård, S. Weizenegger, T. Fechtenburg, Overview of Frequency Control in the Nordic Power System, Tech. Rep., Nordic Analysis Group, 2022, URL https://www.epressi.com.

[27] ENTSOE, Apendix 1 - Load-Frequency Control and Performance, Tech. Rep., 2004, URL https://eepublicdownloads.entsoe.eu.

[28] Fingrid, Reserve Products and Reserve Market Places, Tech. Rep., 2023, URL https://www.fingrid.fi.

[29] S. Bustamante, J.W. gonzález, G.J. López, H.A. Cardona, UFLS and smart load for frequency regulation in electrical power system: A review, IEEE Access 11 (2023) 110967–110984, http://dx.doi.org/10.1109/ACCESS.2023.3321865.

[30] S. Panagi, A. Lazari, V. Koutsoloukas, P. Aristidou, Impact of fast frequency response on renewable energy source curtailment and load shedding, in: CIRED 2024 Vienna Workshop, 2024.

[31] A. Argyrou, S. Panagi, P. Aristidou, Comparison of fast frequency response methods in the low-inertia grid of cyprus, in: 2024 3rd International Conference on Energy Transition in the Mediterranean Area, SyNERGY MED, 2024, pp. 1–5, http://dx.doi.org/10.1109/SyNERGYMED62435.2024.10799326.

[32] M. Paturet, U. Markovic, S. Delikaraoglou, E. Vrettos, P. Aristidou, G. Hug, Stochastic unit commitment in low-inertia grids, IEEE Trans. Power Syst. (ISSN: 1558-0679) 35 (5) (2020) 3448–3458, http://dx.doi.org/10.1109/TPWRS.2020.2987076.

[33] P. Kundur, Power system stability, Power Syst. Stab. Control. 10 (2007).

[34] Electricity Authority of Cyprus, Generation data, 2023, URL https://www.eac.com.cy.